Research Article | Vol. 28, No. 10 / 11 May 2020 / Optics Express 14209

Optics EXPRESS

Hyperspectral imaging for high-throughput, spatially resolved spectroscopic scatterometry of silicon nanopillar arrays

BRIAN GAWLIK,[1,2,*] CRYSTAL BARRERA,[1,2] EDWARD T. YU,[1,3] AND S. V. SREENIVASAN[1,2]

[1]NASCENT Center, The University of Texas at Austin, Austin, Texas 78705, USA
[2]The University of Texas at Austin, Dept. of Mechanical Engineering, Austin, Texas 78705, USA
[3]The University of Texas at Austin, Dept. of Electrical and Computer Engineering, Austin, Texas 78705, USA
*brian.gawlik@utexas.edu

Abstract: Modern high-throughput nanopatterning techniques, such as nanoimprint lithography, make it possible to fabricate arrays of nanostructures (features with dimensions of 10's to 100's of nm) over large area substrates (cm^2 to m^2 scale) such as Si wafers, glass sheets, and flexible roll-to-roll webs. The ability to make such large-area nanostructure arrays (LNAs) has created an extensive design space, enabling a wide array of applications including optical devices, such as wire-grid polarizers, transparent conductors, color filters, and anti-reflection surfaces, and building blocks for electronic components, such as ultracapacitors, sensors, and memory storage architectures. However, existing metrology methods will have trouble scaling alongside fabrication methods. Scanning electron microscopy (SEM) and atomic force microscopy (AFM), for instance, have micron scale fields of view (FOV) that preclude comprehensive characterization of LNAs, which may be manufactured at m^2 per minute rates. Scatterometry approaches have larger FOVs (typically 100's of μm to a few mm), but traditional scatterometry systems measure samples one point at a time, which also makes them too slow for large-scale LNA manufacturing. In this work, we demonstrate parallelization of the traditional spectroscopic scatterometry approach using hyperspectral imaging, increasing the throughput of the technique by a factor of 10^6-10^7. We demonstrate this approach by using hyperspectral imaging and inverse modeling of reflectance spectra to derive 3-dimensional geometric data for Si nanopillar array structures over both mm and cm-scale with μm-scale spatial resolution. This work suggests that geometric measurements for a variety of LNAs can be performed with the potential for high speed over large areas which may be critical for future LNA manufacturing.

1. Introduction

Modern high-throughput nanopatterning techniques such as nanoimprint lithography [1] make it possible to fabricate arrays of nanostructures (features with dimensions of 10's to 100's of nm) over large area substrates (cm^2 to m^2 scale) such as Si wafers, glass sheets, and flexible roll-to-roll webs. The ability to make such large-area nanostructure arrays (LNAs), has created an extensive design space enabling a wide array of applications. For instance, LNAs exhibit nanophotonic properties enabling optical devices such as wire-grid polarizers (WGPs) [2], transparent conducting metal mesh grids (MMGs) [3–5], color filters [6–8], perfect mirrors [9], and anti-reflection surfaces [10–14]. LNAs can also be utilized for increasing surface area as well as generally creating large arrays of discrete features to be utilized as building blocks for electronic components in memory storage devices [15–17], sensors, and microprocessors. Si nanopillar/nanowire arrays, for instance, are being researched for a variety of applications including gas sensing [18–20], optical sensing [21–23], battery technology [24], ultracapacitors

#388158 https://doi.org/10.1364/OE.388158
Journal © 2020 Received 15 Jan 2020; revised 23 Feb 2020; accepted 23 Feb 2020; published 27 Apr 2020

Optics EXPRESS

[25,26], memory [15–17], as well as color filtering for printing [6,8], displays, and imaging devices [23].

With increasing deployment of nanofabrication methods for high-volume manufacturing of LNAs for these applications, there is an accompanying need for high throughput nanoscale metrology. Unfortunately, current metrology methods are not directly suited for scaling to very high manufacturing throughput. Historically, particularly in the semiconductor industry, the primary metrology approach for all things micro – and eventually nano – has been microscopy. Techniques like scanning electron microscopy (SEM) and atomic force microscopy (AFM) have been used extensively. However, microscopy approaches don't apply well to LNAs, because their throughput is extremely low due to their limited fields of view (FOVs) which are micron-scale. Furthermore, 3-dimensional SEM measurements often require sample destruction – such as in the case of cross-sectional SEM – which makes it ineffective for quality inspection of outgoing products.

Scatterometry is an optical metrology technique used extensively by the semiconductor industry that allows for non-destructive geometric characterization at relatively fast speeds and large areas compared to microscopy approaches [27,28]. Scatterometry measures angle (angular) or wavelength (spectroscopic) resolved reflectance or transmittance from nanostructure arrays, typically with a spot size of 100's of μm to a few mm, and infers the average local geometry of the features through inverse modeling of the features' optical behavior using numerical simulation methods like rigorous coupled wave analysis (RCWA) or finite difference time domain (FDTD). Compared to microscopy, the FOV of scatterometry is relatively large, however, the spot size is still very small compared to the potentially m^2 areas of LNAs, and since traditional scatterometry systems are limited to measuring in a serial point-to-point fashion, they would still be very slow in this context.

Traditional scatterometry techniques can be parallelized using imaging methods [29–31] which can dramatically increase their measurement throughput. Spectroscopic scatterometry can be readily extended to imaging using existing hyperspectral imaging approaches. Angular scatterometry can be performed in an imaging fashion as well, although there are fundamental limitations with oblique imaging. Some of these can be mitigated - for instance, focusing issues can be solved using Scheimpflug imaging [29] - but the image pixels will inherently become increasingly rectangular as the angle increases. For these reasons, it may be preferred to use the spectroscopic approach when imaging scatterometry is desired. However, angular scatterometry may be fundamentally preferred in situations when structure reflectance has considerably more sensitivity to angle than to wavelength, or when accurate material data across a range of wavelengths is not available. Regardless, hyperspectral imaging allows for relatively seamless extension of the spectroscopic approach, and in the context of well-characterized materials like Si, the approach is very attractive due to the advantages of imaging.

In this work, we demonstrate that imaging spectroscopic scatterometry applied to arrays of Si nanopillars enables feature geometry at the nanoscale to be determined over mm and cm-scale areas with μm-scale spatial resolution. The highly parallel nature of imaging implies significant throughput advantages and we show how the spatially resolved measurement can reveal subtle geometric variations that would otherwise be missed with traditional point measurements.

2. Methods

2.1. Experimental setup

The wafer scale hyperspectral imaging system for reflective measurements used here is shown in Fig. 1(a). The system uses a Tunable Light Source from Newport (model# TLS-300X) which directs light from a xenon arc lamp through a monochromator, producing a beam of light which is tunable to different spectral bands in the visible spectrum and beyond. The beam is collimated by an achromatic doublet lens and then split by a beamsplitter. One half of the beam is directed

Optics EXPRESS

downwards towards reflective samples which rest on a flat stage. Having a collimated beam incident on the sample allows for large FOV and also creates a situation which is very similar to the plane wave approximation used in the FDTD reflectance simulations. The collimated beam is reflected from the sample, passes again through the beamsplitter, and enters a telecentric lens attached to a 5-megapixel monochromatic CMOS camera from FLIR (#CM3-U3-50S5M). Lens telecentricity assures uniform angular collection over the entire field of view. The system uses either a 0.367X lens (Edmund Optics #88-602) or a 3X lens (Edmund Optics #63-738) which produce FOVs of 19×23 mm and 2.4×2.8 mm respectively and pixel sizes of 9.4 μm and 1.2 μm respectively. The actual spatial resolution of the system is ~2-3 times larger than the pixel size for either lens.

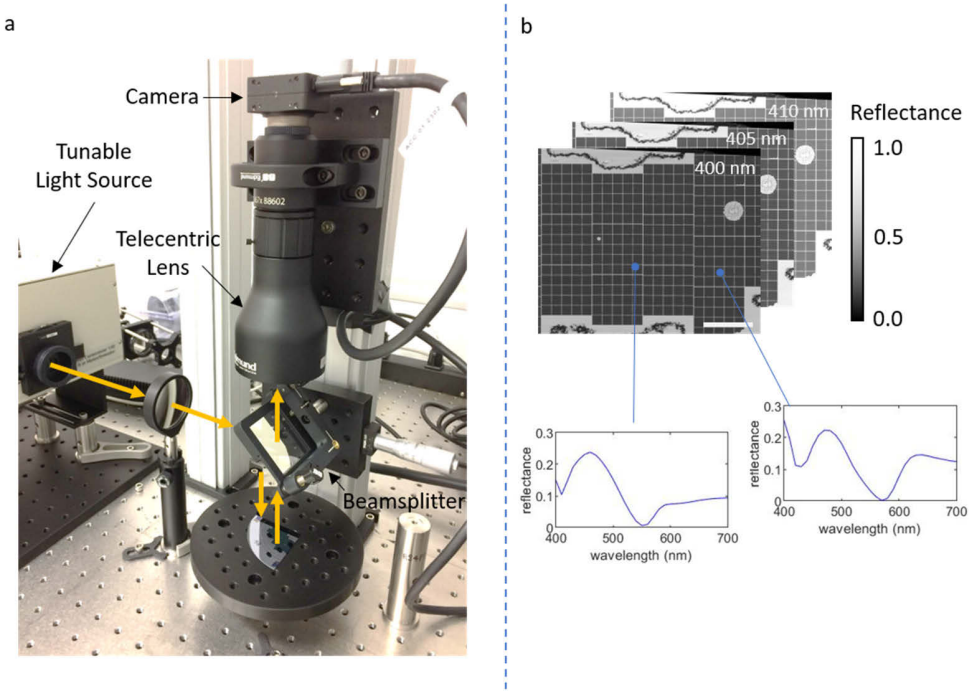

Fig. 1. (a) Wafer scale hyperspectral imaging system for reflective measurements with beam path indicated by the yellow arrows. (b) Conceptual illustration of hyperspectral reflectance image.

Typically, images are taken across the 400 to 700 nm wavelength range in steps of 5 nm (each having spectral bandwidth of 8 nm) producing 61 different images. The raw image intensities of the sample are calibrated using corresponding images of a reference bare Si wafer, producing reflectance images, whose values are scaled from 0 to 1, at each spectral band. Alternatively, the dataset can be thought of as being an image in which there is a reflectance spectrum located at every pixel. A conceptual illustration of the hyperspectral reflectance image is shown in Fig. 1(b).

2.2. Sample fabrication

In this work, Si nanopillar arrays are fabricated using the process flow shown schematically in Fig. 2. The first sequence in the process flow is nanoimprint patterning performed using jet and flash imprint lithography (JFIL) [1] in which the features are defined in an imprint resist mask. Once the imprint process has been completed, a "descum" reactive ion etch (RIE) process (O_2 and Ar) is performed to remove the thin layer of resist, called the residual layer thickness (RLT),

Optics EXPRESS

that remains between the features, exposing the underlying SiO_2 hardmask. After the descum etch, the pattern is transferred to an SiO_2 hardmask using an RIE process (CF_4, Ar, and CHF_3). Finally, the pattern is transferred into the c-Si substrate using another RIE process (HBr and Cl_2). During the RIE steps, a significant sidewall angle is imparted to the features, and thus the final Si features typically have a truncated cone shape. Note that any remaining hardmask and/or resist mask on the pillars after the Si etch is removed using subsequent piranha and HF cleaning processes.

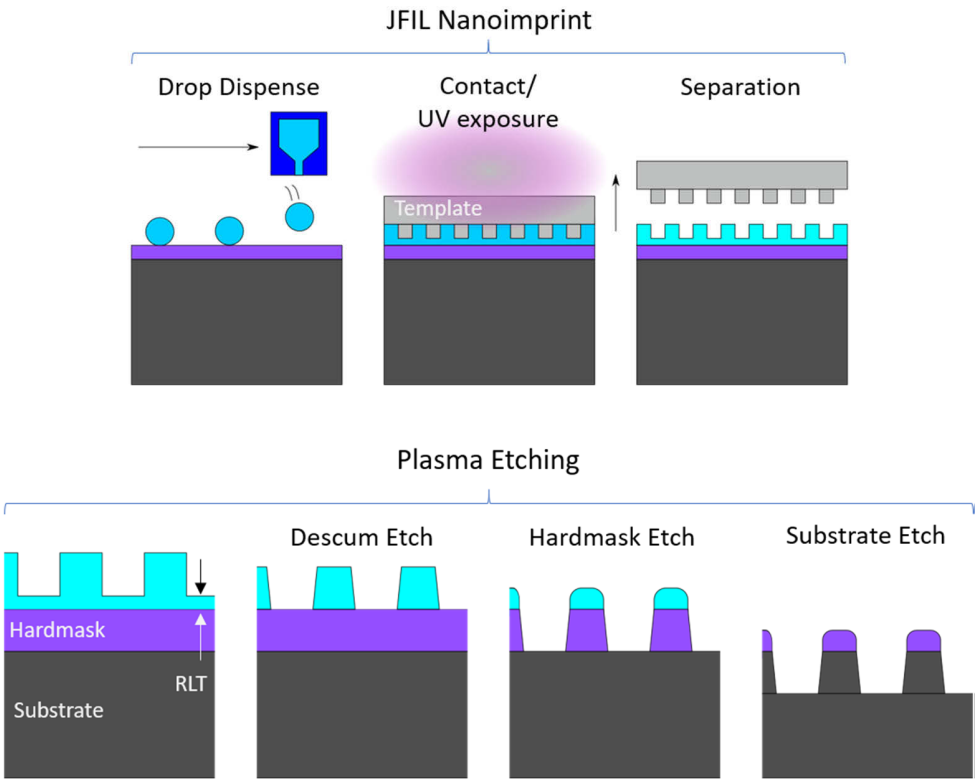

Fig. 2. Exemplar nanomanufacturing process flow enabled by Jet and Flash Imprint Lithography (JFIL) [1] and plasma etching.

The template used here imprints pillars that have a nominal feature diameter of 130 nm and 200 nm pitch. The pillar arrays are arranged into 1×1 mm squares which are distributed around the template. The groups of 1×1 mm squares can be seen in images of the sample throughout the paper. In between the patterned squares are regions typically referred to as "streets" which contain bare Si and occasionally alignment markers.

3. Results and discussion

3.1. Forward modeling and validation

To demonstrate imaging spectroscopic scatterometry, we apply the technique to a sample of Si nanopillar arrays that we have fabricated (see Section 2). The cross-section SEM images in Fig. 3(b) show the general shape of the structure. We choose to use such a simple structure to keep the generation of the scatterometry library as computationally tractable as possible. A forward model is developed for this structure using Lumerical FDTD with the following geometric parameters: Top diameter (D), height (H), sidewall angle (θ), and native oxide thickness (N.O.)

Optics EXPRESS

as shown in Fig. 3(c). In actuality, the structure appears to be slightly more complex due to the varying sidewall angle seen in the SEM images, but the simplified model presented here is sufficient to capture key aspects of the reflectance spectra and their dependence on the structure of the Si pillars.

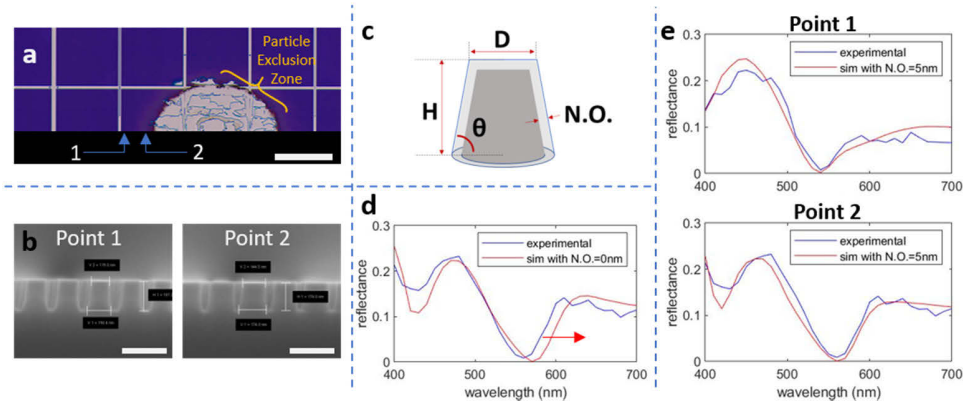

Fig. 3. Si nanopillar forward model validation. (a) RGB image of a nanopillar array sample showing locations of the two cross-section SEM images shown in (b) (scale bar = 1 mm). Note that the photo is not of the cleaved sample itself but is just cropped to show the cleave location. (b) Representative cross-section SEM images corresponding to the points 1 and 2 from (a) (scale bars = 400 nm). (c) Schematic of the nanopillar geometric model showing the various geometric parameters. (d) Plot of simulated reflectance spectra (red) based on the SEM measurements and experimentally measured spectra (blue) with red-shift between experiment and simulation indicated. (e) Plots of reflectance spectra taken at the points 1 and 2 from (a) showing good match between experimental (blue) and simulated spectra (red) based on the SEM measurements with a native oxide thickness of 5 nm.

The forward model is validated by comparing simulated reflectance spectra based on measured geometries from cross-section SEM images taken on the cleaved portion the sample shown in Fig. 3(a) to experimentally measured spectra from the same locations. We chose to take these measurements near an exclusion zone caused by particle contamination during the imprint process to take advantage of the fact that a range of geometries typically exists near the edge of this type of defect, thus providing more thorough validation. As discussed in Ref. [32], a particle causes a transient region where the RLT is thicker resulting in thicker features (in the area of point 2) around the exclusion zone. Representative cross-section SEM images are taken at the points 1 and 2 as shown in Figs. 3(a) and 3(b).

We found that a native oxide layer needed to be added to the model since simulated spectra based on cross-section SEM measurements of the dimensions D, H, and θ yield spectra that are consistently red-shifted from the experimental spectra that are measured by the spectral imaging system as shown in Fig. 3(d). Based on our previous experience [8], we understood that the red-shift was due to the presence of a low index layer comprised of native oxide and/or surface roughness caused by etch damage on the outside of the pillars, creating a core-shell structure. The core-shell structure is not directly observable in the SEM, and only the total diameter can be measured. Thus, the measured diameter is somewhat larger than the actual diameter of the Si core which is what dominates the light interaction. To account for this, we add a native oxide layer to the simulation. A native oxide thickness of 5 nm was found to produce a good match between simulation and experimental spectra based on the two measured points as shown in Fig. 3(e).

Optics EXPRESS

3.2. Inverse modeling and application

Having validated the forward model, a library of simulated spectra is then generated. In order to keep the computation of the library manageable, the model is simplified by removing the low index layer from the simulation. This removes the ability to determine the thickness of the low index shell (assumes it is zero) but remains effective for determining the dimensions of the Si core of the structure. As stated, the Si core dominates the light interaction, such that for a given Si core geometry, adding a thin low index layer on top of it has little effect. Our library is generated based on the following parameter ranges: D: 100-190 nm in steps of 3 nm, H: 150-230 nm in steps of 5 nm, and θ: 80-89° in steps of 1° resulting in a library with 5270 simulated spectra. This geometric range is chosen based on the expected range of geometries on the sample. Once the library is generated, it is used to inversely determine the unknown geometry on a sample of Si nanopillar arrays, knowing the measured reflection across the visible spectrum. The sample, shown in Fig. 4(a), undergoes hyperspectral reflectance imaging and then each of the millions of spectra from the experimental dataset are compared across the entire library to find the best match – the one that produces the lowest root mean square error (RMSE) between simulated and experimental spectra. The geometric parameters corresponding to these best-matching simulations are then taken as the local geometric parameters of the array in each pixel location in the image. The three geometric parameters are plotted in colormaps over the sample as shown in Figs. 4(b)–4(d). Only the square regions containing the pattern are analyzed using scatterometry. Un-patterned regions, like bare Si and the "streets" in between the squares, are masked out of the analysis and indicated by the darker gray color in the colormap. Areas within the patterned regions with an RGB color similar to that of Si are assumed to be Si and left out of the scatterometry analysis and indicated by a lighter gray color. Areas that do not produce a low enough RMSE value to be considered a good match are indicated by the color black. The maximum threshold for a good RMSE is set at 0.03. The RGB image is obtained via transformation of the hyperspectral reflectance image using the CIE 1931 color matching functions [33].

The imaging measurement reveals changes in the various geometric parameters of the array over the sample. For instance, the diameter colormap shown in Fig. 4(b) indicates that the diameter increases significantly as the pattern edges are approached. This diameter increase occurs because of increased imprint RLT near the edges of the pattern, which causes the features in these regions to be larger as a consequence of resist feature shrinkage in areas with thinner RLT during the descum etch. As expected, we also see this diameter increase around the perimeter of exclusion zones in the pattern which were caused by particle contamination during imprinting. At the edges of these particle exclusion zones, the RLT is thicker as a consequence of a particle having raised the template away from the substrate [32]. We also observe that the sidewall angle increases in tandem with the top diameter near the edges of the patterned area and the edges of the particle zones. In some instances, near the top of the pattern, the height increases in tandem with the diameter as well which, based on the typical behavior of the fabrication process flow, is unexpected behavior, although in most areas of the sample the height seems uncorrelated with the diameter variations. This is expected, since diameter variations usually occur due to lithographic issues like RLT variations, which don't affect etch depth except for the case when the RLT is so thick as to delay the etch processes that follow the lithographic step, but this sample does not appear to have experienced much etch delay except for at the very edges of the particle zones.

To provide further validation for the scatterometry results, we obtained cross-section SEM images of the cleaved portion of the sample near the edge of the particle exclusion zone as shown in Fig. 5(a). For this experiment, we take SEM measurements starting at the left edge of the square to the left of the exclusion zone and proceed in 50 μm increments towards the right, approaching the particle exclusion zone. In total, 11 SEM measurements were taken, some of

Optics EXPRESS

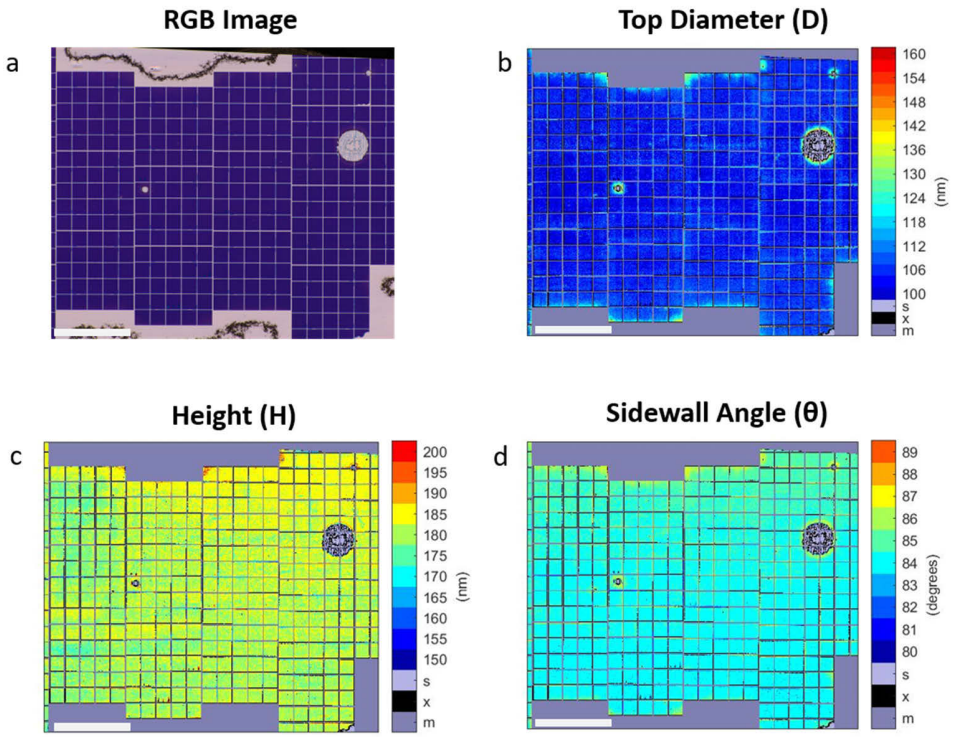

Fig. 4. Scatterometry results for full wafer of Si nanopillar arrays. (a) RGB image of a sample of Si nanopillar arrays. (b) Colormap of scatterometry measured top diameter (D). (c) Colormap of scatterometry measured height (H). (d) Colormap of scatterometry measured sidewall angle (θ). Scale bars are all 5 mm. Each of the colormaps has 3 colors dedicated to results that belong to areas that were masked out of the analysis ("m"), areas that did not produce an acceptable match ("x"), and areas that were determined to be bare Si ("s").

which are shown in Fig. 5(c), for a distance of 500 μm covering the area shown by the yellow bracket in Fig. 5(b).

Comparisons of the SEM measurements and the scatterometry results are shown in Fig. 5(d). The diameters of both the SEM and scatterometry measurements increase in tandem as the edge of the particle exclusion zone is approached, and the quantitative agreement between them is excellent. The SEM diameter is slightly larger than the scatterometry value at all points, but the difference between the two datasets is ~10 nm in diameter which corresponds to the native oxide thickness of 5 nm (radius) that produces a good match to the experimental spectra demonstrating that the 5 nm native oxide assumption works well across a range of top diameter values. The height and sidewall angle values are very similar between SEM and scatterometry. Unlike the diameter, the height should be the same for SEM and scatterometry, because the low index layer should exist equally on the trench floor between the features and on the tops of the features. The sidewall angle measurements should also be unaffected by the low index layer. Interestingly, both systems measure a slight increase in the sidewall angle as the particle zone is approached. It's possible that the etch naturally produces a directly proportional relationship between diameter and sidewall angle, at least for these features and this range of geometric values. Overall, the scatterometry measurements agree well with cross-section SEM measurements.

To estimate the uncertainty of the measurement, we show in Fig. 6 a set of contour plots of RMSE as a function of D, H, and θ for a representative point from the results in Fig. 4. The point

Optics EXPRESS

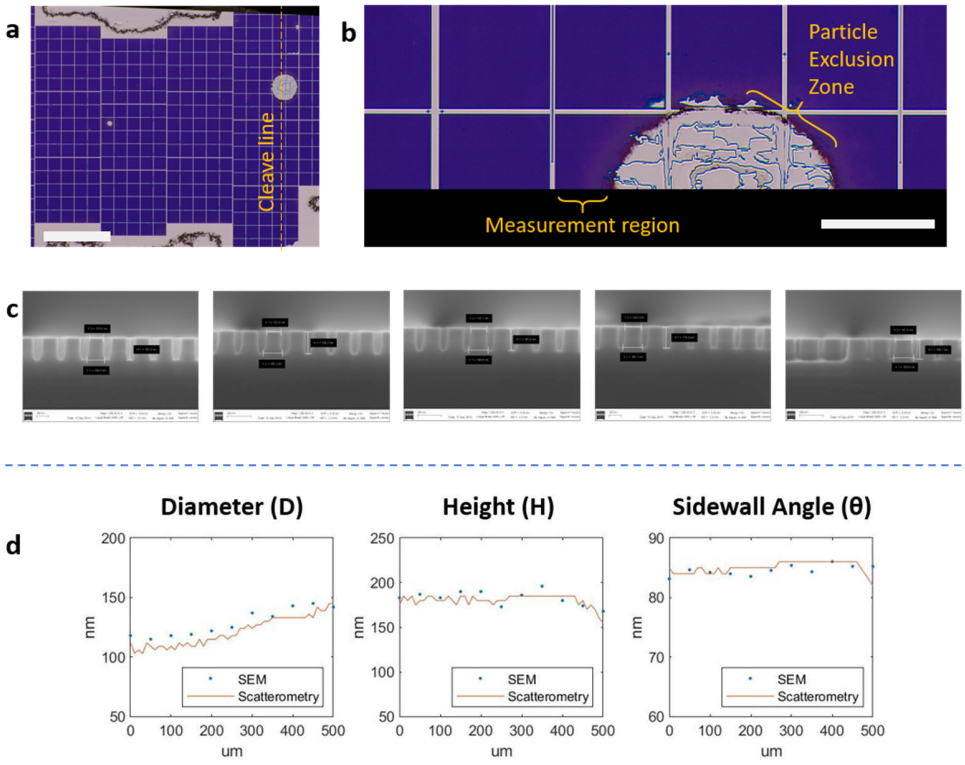

Fig. 5. Comparison of scatterometry to SEM results. (a) RGB image of Si nanopillar array sample showing the line at which it was cleaved for cross-section SEM (scale bar = 5 mm). (b) Cropped RGB image showing the cleaved portion of the sample and the measurement region indicated by the yellow bracket for cross-section SEM measurements which were taken along the edge (scale bar = 1 mm). (c) Examples of cross-section SEM images (every other image) taken left-to-right along the measurement region shown in (b). (d) Plots comparing the results of the cross-section SEM measurements and scatterometry measurements for the three geometric parameters D, H, and θ.

of the best match is indicated by the red "x" and the dotted black line shows where the threshold of an acceptable match (RMSE = 0.03) was set. This threshold includes our estimate of the uncertainty in experimentally measured reflectance values, taken to be ± 0.01. Anything within this contour could have been considered an acceptable match, although the best match in this case has considerably lower RMSE. The uncertainties in the determination of D, H, and θ are then estimated to be on the order of the range that this contour spans for each of the three parameters. In this case, the range for D is ±10 nm, for H is ± 20 nm, and for θ is ± 2°. The sensitivity of the reflectance to these structural parameters is the primary factor governing the uncertainty of the geometric measurement via scatterometry. Other structures, for instance hourglass shaped Si nanopillar resonators [8], have considerably higher sensitivity to dimensional changes, and therefore the uncertainty in the geometric determination for these structures would be less.

3.3. *Detection of imprint template artifact*

A higher magnification spectral image was taken of another sample using a 3X magnification lens, and scatterometry analysis produced the colormaps shown in Fig. 7. Here, the pixel size is about 1.2 µm. Again, only the square regions containing the pattern are analyzed using scatterometry

Optics EXPRESS

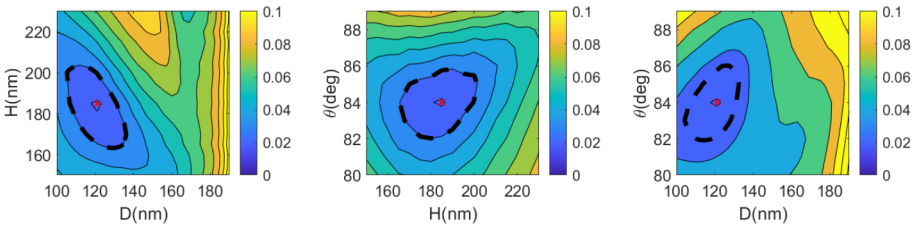

Fig. 6. Contour plots of the RMSE as a function of the three parameters D, H, and θ based on a representative point from Fig. 4. having D=121 nm, H=185 nm, and θ=84°. Because there are three dimensions the plots must be shown with two of the parameters at a time. In each plot, two parameters are shown varying while the third parameter is held constant at whatever its value was for the best match determined by the lookup procedure. The acceptable match threshold of 0.03 is shown by the dotted black line and the location of the best match is indicated by the red "x" marker.

and this time areas that do not produce a good match (RMSE > 0.03) are indicated by the color magenta.

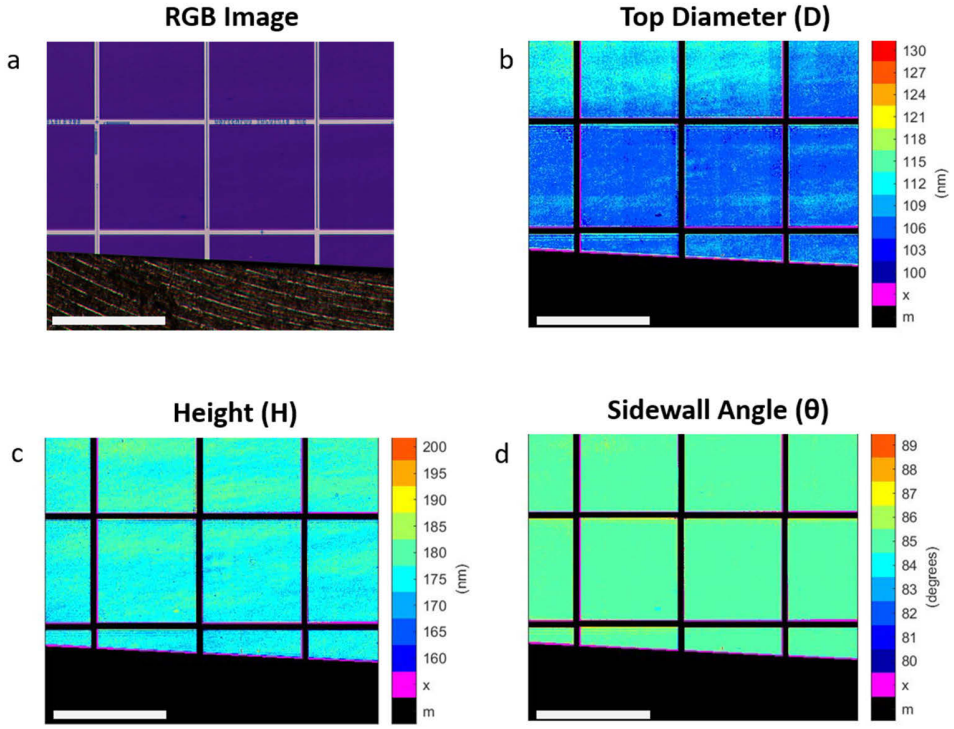

Fig. 7. Scatterometry results for a sample containing Si nanopillar arrays at high magnification. (a) RGB image of a sample of Si nanopillar arrays taken with a 3X magnification hyperspectral imaging system. (b) Colormap of scatterometry measured diameter. (c) Colormap of scatterometry measured height. (d) Colormap of scatterometry measured sidewall angle. Scale bars are all 1 mm. Each of color bar has 2 colors dedicated to results that belong to areas that were masked out of the analysis ("m") and areas that did not produce an acceptable match ("x"). The sample is cut off at the bottom at an angle due to the way it was cleaved.

Optics EXPRESS

The most interesting aspect of this result is the emergence of a square grid pattern exclusively in the diameter colormap with period ~300 μm. We believe this to be an artifact created on the template itself during its fabrication. Template master fabrication is done using electron beam (e-beam) lithography tools which is followed by a template replication step creating daughter templates. These daughter templates are then used to fabricate the silicon wafers used in this study. E-beam lithography tools generally write individual fields with typical size of 100's of μm which are stitched together rectilinearly. It is known that feature size variations can occur over the e-beam write field, causing lateral dimension variations [34]. In this case, diameter is the lateral dimension. Naturally, the height, a dimension defined by etching and not by the lithographic process, should not be influenced by the artifact, and indeed the height does not vary according to the same signature.

These results show the power of using hyperspectral imaging to perform imaging spectroscopic scatterometry measurements. The imaging approach reveals defects that would be impractical to identify using methods such as SEM or traditional non-imaging scatterometry. Detection of the e-beam write field signature, for instance, is only possible by virtue of the spatially resolved data and similar spatial resolution would require serial measurement of millions of individual SEM or point scatterometry measurements to be stitched together. This would be highly impractical for in-line manufacturing diagnostics and even challenging for off-line analysis.

The acquisition of the hyperspectral image using the current system took a few minutes; however, most of this time is due to the slow wavelength switching in the tunable light source. Considering the max framerate of the camera is 30 fps and the exposure times are on millisecond scales, the total hyperspectral image acquisition time can be reduced to ~2 seconds if the wavelength switching is optimized. Also, since fast wafer scanning capabilities exist, there is the potential to quickly image very large areas. It should be noted that computing the library matching procedure for the sample took a considerable amount of time (~5-10 minutes) on a typical PC. This can be sped up using better computational resources as well as more efficient algorithms for the search (e.g. gradient descent or clustering [35]). Furthermore, it would be more practical in a manufacturing scenario to have a hierarchical approach which avoids unnecessary computations by reserving the lookup procedure for areas that have been determined to be defective via, for instance, calculation of RMSE from a single target spectrum.

Naturally, this approach has all of the usual limitations of scatterometry. For instance, the accuracy of the geometric determination is only as good as the forward model being used. In this case, a simplified 3-parameter model was used to limit the computational complexity, but the actual nanopillar structure appears to be slightly more complex. This inherently means that the results are approximate to some extent, although the accuracy ultimately depends on the requirements of the manufacturing tolerances, and this was simply meant to be a demonstration. Also, in scatterometry there is an assumption of uniformity within local groups of pillars existing within a single pixel area that may not actually exist. In fact, the results contain a significant number of "no match" values, particularly at the edges of particle voids where there exists partial breakthrough caused by extreme etch delay. In these areas, the array is not uniform, and this compromises the scatterometry procedure. The effect of longer-range non-uniformity can be mitigated by increasing the spatial resolution of the measurement, but shorter-range non-uniformity can occur over single periods, in which case this strategy doesn't help. Non-uniform arrays can technically be captured by increasing the complexity of the scatterometry forward model to capture multiple periods of the array with varying geometry, but the potential complexity of such a model would increase computational expense dramatically.

Optics EXPRESS

4. Conclusions

These results demonstrate massive parallelization of traditional spectroscopic scatterometry metrology using hyperspectral imaging. This approach is valuable, because it enables scatterometric measurements at much higher throughput while simultaneously providing high spatial resolution, which allows for detection of specific types of patterning defects that would be impractical to obtain using traditional non-imaging scatterometry measurements as well as microscopy measurements. The capabilities of this approach do not transcend the usual fundamental limitations of scatterometry, but nonetheless offer a very useful extension.

The demonstrations that were provided dealt exclusively with wafer samples, although a large portion of LNA manufacturing is expected to take place on roll-to-roll (R2R) systems in the near future. For the case of continuously moving webs, hyperspectral linescan imaging, done either with imaging spectrometers [36,37] or linear variable filter cameras [38,39], should offer a similarly seamless extension for spectroscopic scatterometry. As discussed, the extension of angular scatterometry to imaging involves fundamental challenges which may be further complicated in the context of R2R manufacturing. Whereas wafers, by virtue of their discrete nature, can be rotated to assist with angular measurements, R2R web roller systems are relatively bulky and therefore metrology systems must adapt to the fixed web system. An in-line R2R angular scatterometry approach has been developed which, using scanning optics, can collect angular spectra from individual points at kHz frequencies allowing it to measure while the web is moving [40]. Though fast compared to traditional angular systems, this system still measures the web point-by-point and would require thousands of individual beam paths to provide high spatial resolution measurements. There may be a way to extend this technology to linescan imaging, but to our knowledge this has not been demonstrated. For the time being, hyperspectral imaging and in-line angular scatterometry can be used as complimentary techniques. One approach would be to use hyperspectral imaging for the throughput advantage it offers. Angular scatterometry can then be used as a complement at lower throughput to provide calibrating measurements for structures lacking spectral sensitivity, or where uncertainty may exist in material index data over large spectral ranges.

Funding

National Science Foundation (ECCS-1120823, ECCS-1542159, EEC-1160494).

Acknowledgments

This work was performed in part at the University of Texas Microelectronics Research Center, a member of the National Nanotechnology Coordinated Infrastructure (NNCI), which is supported by the National Science Foundation. We would like to thank the T.W. Whaley, Jr. Friends of Alec Endowed Scholarship for funding Brian throughout multiple semesters.

Disclosures

The authors declare that there are no conflicts of interest related to this article.

References

1. S. V. Sreenivasan, "Nanoimprint lithography steppers for volume fabrication of leading-edge semiconductor integrated circuits," Microsyst. Nanoeng. **3**(1), 17075 (2017).
2. S. H. Ahn, S. Yang, M. Miller, M. Ganapathisubramanian, M. Menezes, J. Choi, F. Xu, D. J. Resnick, and S. V. Sreenivasan, "High-performance wire-grid polarizers using jet and Flash^{TM} imprint lithography," J. Micro/Nanolith. MEMS MOEMS **12**(3), 031104 (2013).
3. R. M. Pallares, X. Su, S. H. Lim, and N. T. K. Thanh, "Fine-tuning of gold nanorod dimensions and plasmonic properties using the Hofmeister effects," J. Mater. Chem. C **4**(1), 53–61 (2016).

Optics EXPRESS

4. P. B. Catrysse and S. Fan, "Nanopatterned Metallic Films for Use As Transparent Conductive Electrodes in Optoelectronic Devices," Nano Lett. **10**(8), 2944–2949 (2010).
5. J. van de Groep, P. Spinelli, and A. Polman, "Transparent Conducting Silver Nanowire Networks," Nano Lett. **12**(6), 3138–3144 (2012).
6. J. Proust, F. Bedu, B. Gallas, I. Ozerov, and N. Bonod, "All-Dielectric Colored Metasurfaces with Silicon Mie Resonators," ACS Nano **10**(8), 7761–7767 (2016).
7. K. Seo, M. Wober, P. Steinvurzel, E. Schonbrun, Y. Dan, T. Ellenbogen, and K. B. Crozier, "Multicolored Vertical Silicon Nanowires," Nano Lett. **11**(4), 1851–1856 (2011).
8. B. M. Gawlik, G. Cossio, H. Kwon, Z. Jurado, B. Palacios, S. Singhal, A. Alù, E. T. Yu, and S. V. Sreenivasan, "Structural coloration with hourglass-shaped vertical silicon nanopillar arrays," Opt. Express **26**(23), 30952 (2018).
9. P. Moitra, B. A. Slovick, W. li, I. I. Kravchencko, D. P. Briggs, S. Krishnamurthy, and J. Valentine, "Large-Scale All-Dielectric Metamaterial Perfect Reflectors," ACS Photonics **2**(6), 692–698 (2015).
10. S. A. Boden and D. M. Bagnall, "Optimization of moth-eye antireflection schemes for silicon solar cells," Prog. Photovoltaics **18**(3), 195–203 (2010).
11. S. A. Boden and D. M. Bagnall, "Nanostructured biomimetic moth-eye arrays in silicon by nanoimprint lithography," in R. J. Martin-Palma and A. Lakhtakia, eds. (2009), p. 74010J.
12. Y.-F. Huang, S. Chattopadhyay, Y.-J. Jen, C.-Y. Peng, T.-A. Liu, Y.-K. Hsu, C.-L. Pan, H.-C. Lo, C.-H. Hsu, Y.-H. Chang, C.-S. Lee, K.-H. Chen, and L.-C. Chen, "Improved broadband and quasi-omnidirectional anti-reflection properties with biomimetic silicon nanostructures," Nat. Nanotechnol. **2**(12), 770–774 (2007).
13. X. Li, P.-C. Li, L. Ji, C. Stender, C. McPheeters, S. R. Tatavarti, K. Sablon, and E. T. Yu, "Subwavelength nanostructures integrated with polymer-packaged iii–v solar cells for omnidirectional, broad-spectrum improvement of photovoltaic performance," Prog. Photovoltaics **23**(10), 1398–1405 (2015).
14. W.-C. Wang, C.-W. Lin, H.-J. Chen, C.-W. Chang, J.-J. Huang, M.-J. Yang, B. Tjahjono, J.-J. Huang, W.-C. Hsu, and M.-J. Chen, "Surface Passivation of Efficient Nanotextured Black Silicon Solar Cells Using Thermal Atomic Layer Deposition," ACS Appl. Mater. Interfaces **5**(19), 9752–9759 (2013).
15. H. Na and T. Endoh, "A Multi-Pillar Vertical Metal–Oxide–Semiconductor Field-Effect Transistor Type Dynamic Random Access Memory Core Circuit for Sub-1 V Core Voltage Operation without Overdrive Technique," Jpn. J. Appl. Phys. **52**(4S), 04CE08 (2013).
16. H. Chung, H. Kim, H. Kim, K. Kim, S. Kim, K.-W. Song, J. Kim, Y. C. Oh, Y. Hwang, H. Hong, G.-Y. Jin, and C. Chung, "Novel $4F^2$ DRAM cell with Vertical Pillar Transistor(VPT)," in *2011 Proceedings of the European Solid-State Device Research Conference (ESSDERC)* (IEEE, 2011), pp. 211–214.
17. Y. Sun, H. Y. Yu, N. Singh, T. T. Le, E. Gnani, G. Baccarani, K. C. Leong, G. Q. Lo, and D. L. Kwong, "Junction-less stackable SONOS memory realized on vertical-Si-nanowire for 3-D application," in *Proceedings of 2011 International Symposium on VLSI Technology, Systems and Applications* (2011), pp. 1–2.
18. A. Cao, E. Sudhölter, and L. de Smet, "Silicon Nanowire-Based Devices for Gas-Phase Sensing," Sensors **14**(1), 245–271 (2013).
19. C. R. Field, H. J. In, N. J. Begue, and P. E. Pehrsson, "Vapor Detection Performance of Vertically Aligned, Ordered Arrays of Silicon Nanowires with a Porous Electrode," Anal. Chem. **83**(12), 4724–4728 (2011).
20. H. Zhao, "Vertical Silicon Nanowire Arrays for Gas Sensing," 97 (n.d.).
21. H. Park and K. B. Crozier, "Vertically Stacked Photodetector Devices Containing Silicon Nanowires with Engineered Absorption Spectra," ACS Photonics **2**(4), 544–549 (2015).
22. H. Park, Y. Dan, K. Seo, Y. J. Yu, P. K. Duane, M. Wober, and K. B. Crozier, "Filter-Free Image Sensor Pixels Comprising Silicon Nanowires with Selective Color Absorption," Nano Lett. **14**(4), 1804–1809 (2014).
23. H. Park and K. B. Crozier, "Multispectral imaging with vertical silicon nanowires," Sci. Rep. **3**(1), 2460 (2013).
24. W.-K. Kim, S. Lee, D. Hee Lee, I. Hee Park, J. Seong Bae, T. Woo Lee, J.-Y. Kim, J. Hun Park, Y. Chan Cho, C. Ryong Cho, and S.-Y. Jeong, "Cu Mesh for Flexible Transparent Conductive Electrodes," Sci. Rep. **5**(1), 10715 (2015).
25. S. Chang, J. Oh, S. T. Boles, and C. V. Thompson, "Fabrication of silicon nanopillar-based nanocapacitor arrays," Appl. Phys. Lett. **96**(15), 153108 (2010).
26. A. Cherala, M. Chopra, B. A. Yin, A. Mallavarapu, S. Singhal, O. Abed, R. T. Bonnecaze, and S. V. Sreenivasan, "Nanoshape Imprint Lithography for Fabrication of Nanowire Ultracapacitors," IEEE Trans. Nanotechnol. **15**(3), 448–456 (2016).
27. C. Raymond, "Overview Of Scatterometry Applications In High Volume Silicon Manufacturing," in *AIP Conference Proceedings* (AIP, 2005), Vol. 788, pp. 394–402.
28. M. H. Madsen and P.-E. Hansen, "Scatterometry—fast and robust measurements of nano-textured surfaces," Surf. Topogr.: Metrol. Prop. **4**(2), 023003 (2016).
29. S. Liu, W. Du, X. Chen, H. Jiang, and C. Zhang, "Mueller matrix imaging ellipsometry for nanostructure metrology," Opt. Express **23**(13), 17316–17329 (2015).
30. M. H. Madsen and P.-E. Hansen, "Imaging scatterometry for flexible measurements of patterned areas," Opt. Express **24**(2), 1109 (2016).
31. N. A. Feidenhans'l, S. Murthy, M. H. Madsen, J. C. Petersen, and R. Taboryski, "Spatial characterization of nanotextured surfaces by visual color imaging," Appl. Opt. **55**(34), 9719–9723 (2016).

Optics EXPRESS

32. S. Singhal, M. A. Grigas, and S. V. Sreenivasan, "Mechanics-Based Approach for Detection and Measurement of Particle Contamination in Proximity Nanofabrication Processes," J. Micro NanoManuf. **4**(3), 031004 (2016).
33. "Colour matching functions," http://cvrl.ioo.ucl.ac.uk/cmfs.htm.
34. T. R. Groves, "3 - Electron beam lithography," in *Nanolithography*, M. Feldman, ed. (Woodhead Publishing, 2014), pp. 80–115.
35. R. Sabbagh, B. M. Gawlik, S. V. Sreenivasan, A. Stothert, V. Majstorovic, and D. Djurdjanovic, "Big Data Curation for Analytics within the Cyber-Physical Manufacturing Metrology Model (CPM3)," Procedia CIRP (n.d.).
36. Resonon, "Resonon, Inc. Pika XC2 Hyperspectral Imaging Camera | Geo-matching.com," https://geo-matching.com/thermal-multi-and-hyperspectral-cameras/pika-xc2-hyperspectral-imaging-camera.
37. Specim, "An advanced imaging solution is needed for rapid and accurate inspection of the entire surface," https://www.specim.fi/downloads/Colour-and-luminance-inspection-with-Specim-FX10.pdf.
38. Ximea, "XIMEA - New xiSpec Hyperspectral Multi-Linescan Camera model available," https://www.ximea.com/en/products-news/hyperspectral-linescan-camera.
39. Delta, "Hyperspectral Imaging," Delta Optical Thin Film A/S (2017).
40. J. J. Faria-Briceno, R. Zhu, V. Sasidharan, A. Neumann, S. Singhal, S. V. Sreenivasan, and S. R. J. Brueck, "Optical angular scatterometry: In-line metrology approach for roll-to-roll and nanoimprint fabrication," J. Vac. Sci. Technol., B **37**(5), 052904 (2019).